

A radial velocity study of the cataclysmic variable LAMOST J035913.61+405035.0

180201222

Department of Physics and Astronomy, University of Sheffield, Sheffield, S3 7RH, UK

11 June 2024

ABSTRACT

Models describing the evolution of cataclysmic variables are tested using masses which are determined by modelling photometric lightcurves. The assumptions on which these photometric mass models are based can be tested by independent mass-determination studies. Eclipsing systems with visible donor stars provide the perfect test beds for these models, as the component masses can be determined from measurements of the radial velocity of the donor star. Observations of the eclipsing cataclysmic variable LAMOST J035913.61+405035.0 are used to measure the radial velocities of the absorption and emission lines which are believed to trace the motions of the white dwarf and donor stars. Radial velocities of $K_1 = 180 \pm 13 \text{ km s}^{-1}$ and $K_2 = 211 \pm 12 \text{ km s}^{-1}$ are measured from the emission and absorption lines respectively. From these measurements, the component masses are found to be $M_1 = 0.88 \pm 0.12 M_\odot$ and $M_2 = 0.76 \pm 0.11 M_\odot$. These results are in agreement with previous radial velocity measurements of LAMOST J035913.61+405035.0. It was not possible to test the photometric mass determination method as the lightcurve did not clearly show the points of white dwarf ingress and egress. Evidence is provided that the cataclysmic variable evolutionary model is valid for long-period systems, where there are currently few known masses.

Key words: binaries: close – binaries: eclipsing – stars: dwarf novae – novae, cataclysmic variables

1 INTRODUCTION

Cataclysmic variable stars (CVs) are interacting binary stars where material from a Roche-lobe-filling late-type secondary (donor) star is accreted onto a white dwarf star (WD) via a gas stream. In non-magnetic systems, mass transfer occurs via an accretion disc, which resides within the Roche-lobe of the WD primary. In magnetic CVs (mCVs), the WD possesses a strong magnetic field which interacts with the accreted matter, resulting in a partial or absent disc. Eclipsing systems are excellent subjects for determining stellar masses and other parameters which provide clues regarding the mechanisms behind stellar evolution. For a review of CVs, see Warner (1995) and Hellier (2001).

CVs are classified by their outbursts. Novae have the most violent outbursts, described by the thermonuclear runaway model where hydrogen accretes onto the WD surface until it becomes hot enough to fuse (Starrfield et al. 1989). This process is only observed to happen once, and novae differ primarily in the "speed" at which their magnitude rises and then decays (e.g. Horne et al. 1993; Smith et al. 1998; Smith 2006).

Dwarf novae erupt far more frequently but with less energy, typically brightening by 4–5 magnitudes. The canonical dwarf nova is the "U Gem" star, named after its prototype U Geminorum which was discovered by Hind (1856) and later proven to differ from the "classical nova" by Pogson (1857). The dwarf nova outburst mechanism, first developed by Osaki (1974), involves the build up of mass in a viscous disc and subsequent "dumping" of material onto the WD. The release of gravitational potential during this process provides the energy for the outburst. Dwarf nova outbursts show great variability. Periods range from weeks to years and the brightest provide

exciting targets for amateur astronomers. SS Cygni was the second dwarf nova to be discovered (Pickering & Wells 1896) and has been monitored for over a century, providing extensive light curves (see e.g. Hellier 2001; Smith 2006). These light curves vary dramatically (e.g. Buat-Ménard et al. 2001), even for the same star, making them difficult to model and their behaviour hard to predict.

In mCVs, the accreted matter from the donor star interacts with the magnetic field lines of the WD. If the field is strong enough, the gas stream follows the field lines and makes contact with the poles of the WD without forming an accretion disc. The first "polar" to be discovered was AM Her (Tapia 1977), which showed polarisation at optical wavelengths, a behaviour exhibited by magnetic WDs (Angel 1978). In systems with weakly magnetic WDs, a partial, ring-like disc may form with the magnetic field interacting with the inner-disc material.

The evolution of CVs is driven by the loss of angular momentum (AM) (e.g. Rappaport et al. 1983; Paczynski & Sienkiewicz 1983; Spruit & Ritter 1983; Knigge et al. 2011). As the system loses AM, the separation between component stars decreases and the period shortens. For CVs with periods $P \gtrsim 3$ hours, the secondary star is approximately in thermal equilibrium as the thermal (Kelvin-Helmholtz) timescale τ_{KH} is far smaller than the timescale of mass-loss τ_{ML} . Due to this, the star has a main-sequence-like mass-radius relationship, and therefore shrinks in response to mass-loss. For the donor star to fill its Roche-lobe, the Roche-lobe must also shrink, which requires AM loss. The dominant mechanism for AM loss at long periods is magnetic braking (e.g. Schreiber et al. 2010; Zorotovic et al. 2016). As material from the donor star moves away from the centre of mass, it remains coupled with the star's magnetic field and continues to rotate with it - conserving angular velocity.

As a result, the AM of the material increases with distance from the donor star. The material eventually leaves the star's potential well, carrying away AM with it. In a system with strong tidal forces such as an interacting binary, the orbital period matches the rotational period of the donor star (tidal locking). These tidal forces work to keep the system tidally locked by keeping the orbital and rotational period of the donor star the same. AM loss of the secondary star will therefore remove AM from the entire system. This has the effect of driving the system to shorter periods.

In the range $2 \lesssim P \lesssim 3$ hours, very few CVs are observed. This "period gap" is caused by a decrease in AM loss at $P \sim 3$ hours. At this point, the size of the Roche-lobe of the donor star does not decrease as quickly as before. Due to this, the donor star shrinks within its Roche-lobe and mass transfer ceases. The system becomes a detached binary. One theory for the decrease in AM loss postulates that at $P \sim 3$ hours, the donor star has lost sufficient mass that it becomes fully convective (e.g. [Spruit & Ritter 1983](#); [Rappaport et al. 1983](#)). If the magnetic field of the star is generated by a dynamo in the transition zone between the radiative core and convective envelope, then the loss of the transition zone means that the dynamo is also lost (e.g. [Smith 2006](#)). The consequent lack of a magnetic field inhibits magnetic braking, so the Roche-lobe of the donor star can no longer continue to shrink to facilitate mass transfer. The system continues to lose AM via gravitational radiation (the emission of gravitational waves) until $P \sim 2$ hours, when the donor star once again fills its Roche-lobe and mass transfer can continue.

Recent evidence suggests that donor stars do not lose their magnetic fields at this point (e.g. [Wright & Drake 2016](#)). [Garraffo et al. \(2018\)](#) suggest that an increase in the complexity of the magnetic field of the donor star is sufficient to explain the period gap, rather than the total disappearance of the magnetic field. The CV continues to evolve until $P \sim 77$ minutes. At this point (known as the "period bounce"), the mass-loss timescale of the donor star is much shorter than the thermal timescale ($\tau_{KH} \gg \tau_{ML}$) and the star stops contracting in response to mass-loss, increasing the orbital period of the system.

Current CV evolution models are imperfect and lack explanations of various observational data. The model described above does not explain why some CVs are observed in the period gap. Models also predict lower WD masses than are observed (e.g. [Zorotovic et al. 2011](#)) and inaccurate fractions of CVs above and below the period gap and at the period minimum (e.g. [Pala et al. 2020](#)). To match the observational data, additional AM loss is required during CV evolution (e.g. [Schreiber et al. 2016](#)). Increasing the AM loss shortens the mass-loss timescale τ_{ML} , which pushes the secondary star further out of equilibrium. As a result, the star is larger and therefore fills its Roche-lobe at longer periods. The rate of AM loss can be inferred from plots of the secondary mass as a function of the orbital period (e.g. [Knigge et al. 2011](#); [McAllister et al. 2019](#)). Testing these models therefore requires observations of more systems across a range of orbital periods and determination of their masses.

The masses of CV components can be determined by fitting lightcurve models to photometric data (e.g. [Bailey 1979](#); [Smak 1980](#); [Cook & Warner 1984](#); [Wood et al. 1985, 1986](#); [Horne et al. 1994](#); [Littlefair et al. 2008](#); [Copperwheat et al. 2010](#); [Savoury et al. 2011](#)). These models rely on four assumptions, the validity of which require significant testing. These are: the bright spot lies on a ballistic trajectory from the donor star; the donor star fills its Roche-lobe; the WD is accurately described by a known mass-radius relationship; and the whole WD surface is visible and has constant flux. The last assumption is particularly tenuous, as light from the WD may be absorbed by gas in the line-of-sight ([Horne et al. 1994](#)). In addition, emission

from the boundary layer between the inner disc and WD surface may dominate the WD ingress in the observed light curve, instead of the WD surface ([Spark & O'Donoghue 2015](#)). Donor and WD masses obtained with these lightcurve models are used to test CV evolution models and constrain the rates of AM loss (e.g. [Knigge et al. 2011](#); [McAllister et al. 2019](#)). It is therefore important to test the predictions of these models by independently determining component masses.

Component masses can be independently measured through spectroscopic studies of eclipsing CVs. In particular, the absorption lines of visible donor stars trace its radial velocity, which can be used to determine its mass. [Horne et al. \(1993\)](#) measured the component masses, radii, binary separation and inclination of the nova DQ Her from the velocity shift of the NaI doublet at $\lambda \sim 8190$ Å. The individual spectra were cross-correlated with the average spectrum to measure the velocity shift. Similarly, [Smith et al. \(1998\)](#) performed a similar analysis on the old nova BT Mon. However, the NaI doublet in this system was too faint for cross-correlation, so a modified technique was used to determine radial velocities. [Savoury et al. \(2012\)](#) investigated the dwarf nova CTCV J1300-3052 using a technique similar to [Horne et al. \(1993\)](#) and found masses which were in excellent agreement with those determined using a photometric fitting method ([Savoury et al. 2011](#)). Five CVs with component masses found using the photometric fitting method were investigated by [Godon & Sion \(2022\)](#). The observed masses of four of these systems were found to be in good agreement with predictions. However, [Godon & Sion \(2022\)](#) found the predicted mass of the dwarf nova GY Cnc to be too large in contrast to most observations (e.g. [Zorotovic et al. 2011](#)), placing the model assumptions under scrutiny. However, a recent study of GY Cnc has confirmed the mass given by the photometric fitting technique to be correct ([Littlefair et al. 2023](#)), providing further evidence of the reliability of the models.

This study aims to further test CV evolution models by determining the component masses of the eclipsing binary LAMOST J035913.61+405035.0 (hereafter LAMOST 0359) by using a radial velocity technique akin to that of [Horne et al. \(1993\)](#), [Smith et al. \(1998\)](#), [Savoury et al. \(2012\)](#) and [Littlefair et al. \(2023\)](#). LAMOST 0359 was discovered by [Thorstensen \(2020\)](#) in follow-up observations of the Large Sky Area Multi-Object Fiber Spectroscopic Telescope ([Hou et al. 2020](#)). Photometric observations show outbursts and variations in brightness consistent with a Z Cam dwarf nova. [Thorstensen \(2020\)](#) determined that a secondary star of the spectral type $M1 \pm 1$ contributes $V = 20.3$ to the system's brightness. They also note that the system shows outbursts which change the brightness by 2.5 mag, which is lower than typically expected for a dwarf nova but not abnormal. The 5.49-hour orbital period of the system provides a test of the evolutionary model predictions at long periods, where little data is currently available. The aim of this work is to test the evolutionary CV models at long periods. Additional goals are to determine the spectral type of the secondary star and investigate the nature of the WD star, which displays single-peaked emission lines in its spectra.

2 OBSERVATIONS

An observing proposal was submitted in June 2023 for the Intermediate Dispersion Spectrograph (IDS) on the 2.54-m Isaac Newton Telescope at the Roque de los Muchachos Observatory in La Palma. The science case was accepted on the 19th and the technical case on the 21st of June. A total of 60 spectra were taken over three nights on the 8th, 9th and 11th of September 2023 with the IDS Red+2 detector. An entire orbit was covered by observing over these three

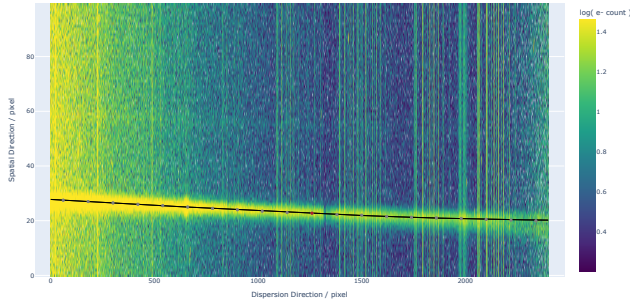


Figure 1. A polynomial fit to one spectrum from the AP_TRACE function in ASPIRED. The black line shows the best fitting trace to cross-correlation peaks of individual subspectra (see text for details).

days. Exposure times of 600 seconds were used and the readout time was around 42 seconds. Comparison arc spectra were taken with a combination of CuNe and CuAr lamps both before twilight and then every hour (every six exposures) to calibrate flexure, adding around 10 minutes of additional overhead time. A R400R grating was used, giving an unvignetted wavelength range of 5545 - 8955 Å for a 1-arcsecond slit-width with a resolution of 3.1 Å (128 km s⁻¹). One standard star was observed on each of the three observing nights. The standards are shown in Table 1. Humidity and dust varied over the three nights. Night two experienced periods of high dust and humidity, and on night three the humidity was high. Seeing over the three nights ranged between 1 and 1.5 arcseconds.

Photometric observations were also taken on the night of the 19th of November, 2023 using ULTRASPEC (Dhillon et al. 2014) on the 2.4-m Thai National Telescope at Doi Inthanon in Thailand. These observations were taken using the SDSS g-band filter with an exposure time of 4.7 seconds. The sky was photometric. Flat fielding, de-biasing and aperture photometry were carried out using the HiPERCAM data reduction pipeline¹. The lightcurve was reduced and provided to the author by S. Littlefair².

3 DATA REDUCTION AND ANALYSIS

Data reduction was carried out using the ASPIRED reduction package (Lam et al. 2023) in PYTHON. Pixel-to-pixel variations were corrected with a bias-subtracted tungsten lamp flat-field. The AP_TRACE function was used to identify and trace each spectrum in the raw data. Each spectrum was divided into several subspectra and summed in the direction of dispersion to improve the signal-to-noise ratio (S/N) and generate a line-spread function. Each line-spread function was cross-correlated with that of the adjacent subspectrum. A polynomial was then fit to the shifts from the cross-correlation, which traces the spectrum. An example of the polynomial fit to a spectrum is shown in Fig. 1.

Spectra were then optimally extracted using a technique developed by Horne (1986) with the AP_EXTRACT function. The sky background was estimated to be 50% of the peak brightness for the science images and 5% for the standards. Fig. 2 gives an example of the extraction of

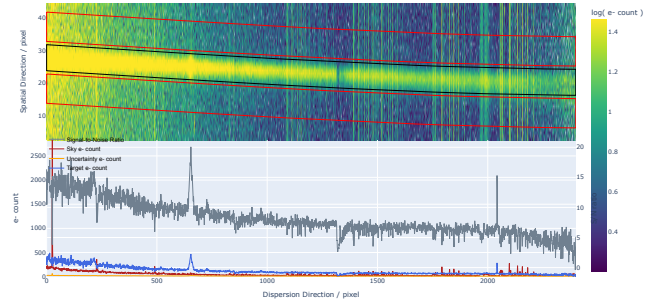


Figure 2. The extraction of a science frame spectrum. Upper panel: The blue box traces the area from which the spectrum data is extracted using the optimal extraction method of Horne (1986). The red boxes above and below the spectrum indicate the area from which the sky background is extracted. Lower panel: The extracted spectrum is plotted as a function of the pixel value of the detector. The spectrum is shown as a solid blue line. ASPIRED also shows the calculated sky background (red) and signal-to-noise (grey) from the extraction.

a science image. The sky background is extracted above and below the spectrum.

Wavelength calibration was carried out using RASCAL (Song et al. 2018,³) within ASPIRED. The CuAr+CuNe lamp arcspectrum which was closest in time and taken at the same telescope pointing as each science frame was used to calibrate for flexure. No arc was observed at the same sky rotation as the standard star exposure on night two. Instead, the 10 second twilight arc was used for the flux calibration of this frame. The set of pixel-wavelength pairs which best fit a polynomial and satisfied given tolerances on the residuals were identified automatically. The best fitting pairs for an example spectrum are shown in Fig. 3. A comparison of the pixel-wavelength pairs with the matching arc lines, the residuals, and the wavelength-pixel fit show a strongly linear relationship. However, this might be an over-estimate of the number of fitting pixel-wavelength peaks. The large number of spectral lines in the CuAr and CuNe atlases ensure that RASCAL has a high chance of finding a wavelength-pixel pair which satisfies the given tolerances. Due to this, the shape of the wavelength-pixel relationship is not necessarily perfect.

The spectrum of each observed standard star was smoothed with a Savitzky-Golay filter (Savitzky & Golay 1964) and divided by literature values to obtain a sensitivity function for each night. Strong spectral features around 6550, 6900 and 7640 Å were masked out of this calibration. The appropriate sensitivity function was applied to each science frame.

The TelFit⁴ package in PYTHON (Gullikson et al. 2014) was used to correct for atmospheric absorption in the spectra. A model spectrum was created using the Line By Line Radiative Transfer Model (Clough et al. 2005) and best-fitting parameters found for each spectrum. The humidity varied greatly on each night, so the input parameter used for the atmospheric model was 50%. The resulting correction for one spectrum can be seen in Fig. 4. Due to low S/N, the corrected spectra were sorted by phase into 10 bins. The spectra in each phase bin were resampled onto the same wavelength axis

¹ <http://www.vikdhillon.staff.shef.ac.uk/hipercam/pipeline/index.html>

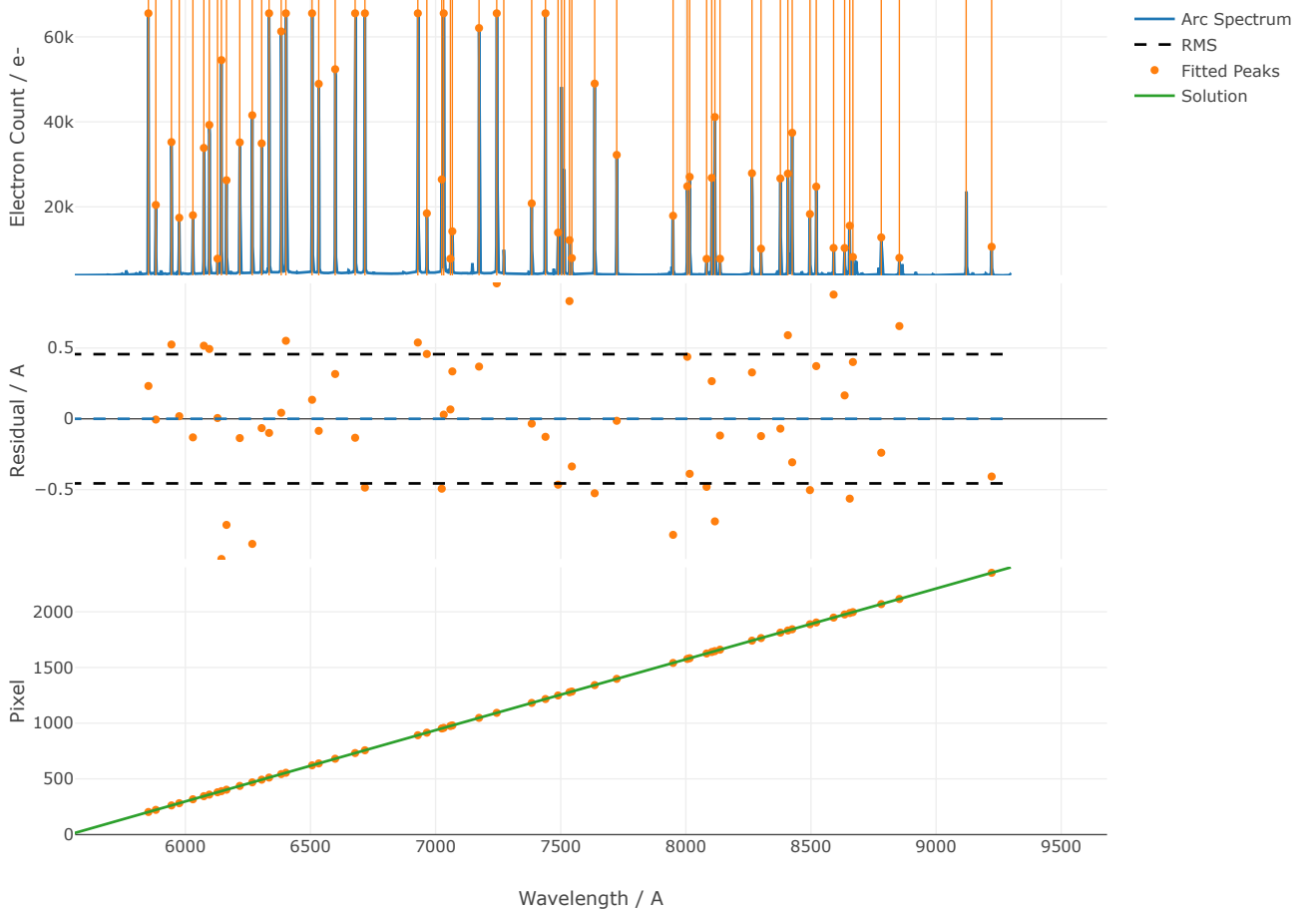
² s.littlefair@sheffield.ac.uk

³ <https://rascal.readthedocs.io/en/latest/>

⁴ <https://telFit.readthedocs.io/en/latest/>

Table 1. Standard stars observed during the September observing run.

NIGHT OBSERVED	ING NAME	OTHER NAME	RA (B1950)	DEC
08/09/2023	SP0146+133	Feige 15	01h 46m 28.4s	+13° 18' 18"
09/09/2023	SP0305+261	HD 19445	03h 05m 28.6s	+26° 09' 06"
11/09/2023	SP2341+322	L1512-34	23h 41m 21.0s	+32° 16' 10"

**Figure 3.** The RASCAL solution to the wavelength calibration for one spectrum. Top: The CuAr+CuNe arc lines are shown in blue and the best-fit pixel-wavelength pairs are shown as orange points. Middle: The scatter of the fitted peaks in angstroms, relative to the true wavelengths. Bottom: A fit to the peaks gives the pixel-wavelength function used for the wavelength calibration.

and the mean spectrum calculated using the `Spectrum1D` function in `SPECUTILS`. This increased the S/N from LAMOST 0359.

4 RESULTS

4.1 Average spectrum

The 10 phase-binned spectra were normalised and corrected for the velocity shift from the motion of the donor star. Normalisation was done by dividing by the mean flux of each spectrum. A fit to the

velocity shifts of the TiO bands (see Section 4.3) was used to find the velocity shift for each phase in the phase bin. The corrected spectra were then resampled onto the same wavelength scale. The mean flux of these corrected spectra is shown in Fig. 5.

Balmer lines are common accretion disc features in CV spectra. The only visible balmer line within the wavelength range of Fig. 5 is the $H\alpha$ peak at 6563 Å, which is strong and single-peaked. Horne & Marsh (1986) showed that typical spectra of high-inclination accreting binaries have double-peaked lines due to the rotation of the disc. The single peaks may indicate a system with a magnetic WD,

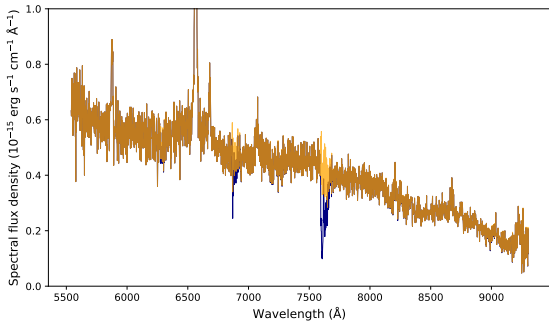


Figure 4. An example of the telluric correction of a single spectrum. The reduced spectrum is shown before and after the correction. The uncorrected spectrum is shown in blue, and has two clear absorption features at ~ 6900 Å and ~ 7600 Å. The corrected spectrum is shown in yellow, where the absorption features are subtracted out.

or where illumination from the WD causes a disc wind (Murray & Chiang 1997).

Three HeI lines are visible in the mean spectrum at wavelengths 5875, 6678 and 7065 Å. The peaks at 5875 and 6678 Å are strong and single-peaked, similar to the H α emission feature. However, the 7065 Å line appears to be double-peaked, suggesting that it originates from a different place to the more energetic HeI lines. The peak at 5875 Å is in the shape of an inverse P Cygni profile, however, this is actually the coincidence of a NaI absorption line with the HeI peak. The spectrum does not cover short enough wavelengths to see a HeII peak at 4685 Å, which would be an indicator of a strong WD magnetic field.

A TiO absorption band is visible at around 7180 Å. This is a common absorption feature of CV donor stars and can be used to track its motion (e.g. Littlefair et al. 2023). The region around 7600 - 7900 Å was affected by atmospheric absorption (see Section 3). Within this region lies another TiO band and the KI doublet at 7664 and 7699 Å. The features are faint, if visible, due to the surrounding noise from the imperfect telluric correction.

The NaI absorption doublet at 8183 and 8194 Å is commonly used to trace the motion of the donor star (e.g. Horne et al. 1993; Savoury et al. 2012). However, the average spectrum shows no sign of these absorption lines. Around this wavelength is the Paschen bump, which appears as a double-peaked emission feature and obscures the NaI line.

The CaII triplet at 8498, 8542 and 8662 Å is seen as emission lines in the mean spectrum. Absorption features from the donor star can be used to find its radial velocity. Emission features arise from irradiation onto the donor star and disc from the WD. Savoury et al. (2012, Fig. 4) see both emission and absorption features in their observations of CTCV J1300-3052.

4.2 Radial velocity of the primary star

The radial velocity of the WD was measured by modelling the velocity shift of the CaII emission lines. It is assumed that these lines originate from the inner disc as a result of irradiation from the WD so that they approximately trace its motion. An average spectrum was created from the mean flux of the phase-binned spectra, which were uncorrected for the velocity shifts. A Gaussian fit was applied to the CaII peak at 8662 Å of this average spectrum. The peaks at

8498 and 8542 Å were not prominent enough for good fits to be made for the phase-binned spectra. The model was applied to each phase-binned spectrum and the wavelength shift $\Delta\lambda$ was calculated from the difference between the mean wavelength of the Gaussian fit to the CaII peak of the individual spectrum, and the rest wavelength of the CaII peak (8662 Å). The velocity shift was then found with the equation:

$$\frac{\Delta\lambda}{\lambda_0} = \frac{v}{c},$$

where v is the velocity shift corresponding to $\Delta\lambda$, λ_0 is the rest wavelength, and c is the speed of light in a vacuum.

These velocity values were then plotted as a function of orbital phase, and can be seen in Fig. 6. The radial velocities were fit with the equation:

$$V(\phi) = \gamma + K \sin[2\pi(\phi - \phi_0)], \quad (1)$$

where γ is the systemic velocity of the system, K is the radial velocity, ϕ is the orbital period, and ϕ_0 is the phase offset. The fit shown in Fig. 6 yields a systemic velocity of $\gamma = 205 \pm 9$ km s $^{-1}$ and radial velocity $K_1 = 180 \pm 13$ km s $^{-1}$.

4.3 Radial velocity of the secondary star

The radial velocities of the secondary star were found by cross-correlating absorption features originating from the secondary star with a solar-metallicity template of a M1 star from Kesseli et al. (2017). The TiO bands were used to trace the motion of the secondary star as the shape remained relatively consistent, and the absorption features could be detected in each of the phase-binned spectra. The template and phase-binned spectra were cropped around these absorption features, then normalised by dividing by the mean flux. A first-order polynomial was then subtracted from the continuum. A low-order fit to the spectrum was used to ensure the shape of the spectra were not altered by the continuum subtraction. The template and phase-binned spectra were then resampled onto the same wavelength scale and apodised to reduce edge effects.

The velocity shifts of the TiO bands were found by fitting a parabola to the three points nearest to the peak of the cross-correlation values. The shifts in velocity of the cross-correlation peaks are sinusoidal in shape, and can be seen in Fig. 7. The radial velocities were found with equation (1) using an iterative fitting method. An initial sinusoidal fit was applied to the data and the residuals calculated by subtracting this fit from the data. A second fit was then applied to radial velocities within 50 km s $^{-1}$ of the original sinusoid. The second iteration gives a systemic velocity of $\gamma = -58 \pm 9$ km s $^{-1}$ and radial velocity of the secondary star $K_2 = 211 \pm 12$ km s $^{-1}$.

4.4 Component masses

The component masses were determined using Kepler's third law:

$$\frac{K_2^3 P_{\text{orb}}}{2\pi G} = \frac{M_1 \sin^3(i)}{(1+q)^2}, \quad (2)$$

where P_{orb} is the orbital period, G is the gravitational constant, M_1 is the mass of the primary star, i is the inclination of the system and q is the ratio of the secondary and primary masses. Due to the unique relationship between $\Delta\phi_{1/2}$, q and i , the mass ratio q can be found for given values of $\Delta\phi_{1/2}$ and i , using a model of the binary star.

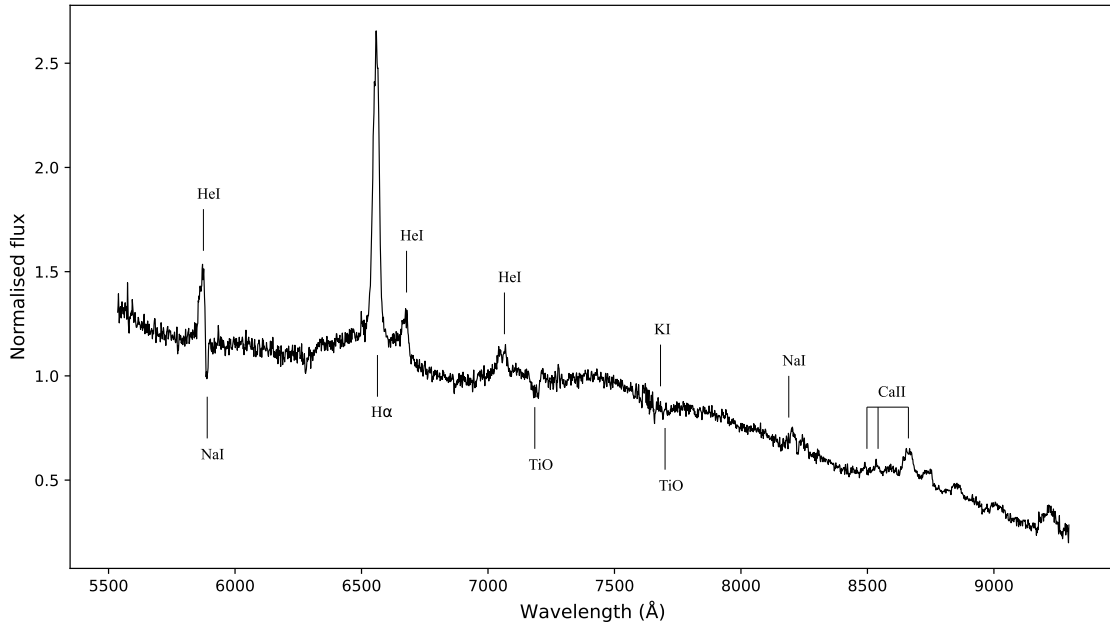


Figure 5. The average spectrum of LAMOST 0359. Each phase-binned spectrum was normalised by dividing by its mean flux. The spectra were then resampled onto the same wavelength axis and then averaged. The NaI, TiO, and KI absorption features and HeI, H α and CaII emission features are labelled. There is evident noise around 7600 Å where the telluric correction has been made, showing that the process was not perfect.

The model was created using Tom Marsh’s `trm.Roche`⁵ function in PYTHON.

The value of $\Delta\phi_{1/2}$ was measured from the lightcurve of LAMOST 0359 which is shown in Fig. 8. There are no clear features indicating the WD ingress and egress. Instead, the width of the eclipse at mid-light was taken to be $\Delta\phi_{1/2}$. The mid-light level was defined as the difference between the minimum and continuum light level. The minimum light was found by fitting a Gaussian curve to the bottom of the trough, and taking the minimum value. The continuum light level was estimated by-eye, by taking a maximum and minimum guess. A fit to the continuum yielded a value for the mid-light level within the range found using the guess values, but the guess values were used to measure $\Delta\phi_{1/2}$ to reflect the uncertainty in this measurement.

The value of $\Delta\phi_{1/2}$ was determined by finding the width of the smoothed lightcurve at the mid-light level. With this technique, the eclipse-width was found to be $\Delta\phi_{1/2} = 0.058 \pm 0.004$. From the measured values of K_2 and $\Delta\phi_{1/2}$, the component masses M_1 and M_2 were plotted as a function of the orbital inclination in Fig. 9.

Singular values for M_1 and M_2 could also be found using the radial velocity of the primary star. Assuming that the radial velocity of the emission lines are equal to that of the WD ($K_1 = K_{WD}$), then the mass ratio can be written as:

$$q = \frac{K_1}{K_2}.$$

Using this value of q , an exact value for the orbital inclination was found using the binary star model. This value of $i = 72.4 \pm 0.7$ degrees is shown on Fig. 9 as a grey band, and corresponds to component masses of $M_1 = 0.88 \pm 0.12 M_\odot$ and $M_2 = 0.76 \pm 0.11 M_\odot$.

⁵ github.com/trmarsh/trm-roche

Table 2. Summary of results from this paper.

Parameter	Value	Unit
K_1	180 ± 13	km s^{-1}
K_2	211 ± 12	km s^{-1}
$\Delta\phi_{1/2}$	0.058 ± 0.004	
i	72.4 ± 0.7	degrees
q	0.86 ± 0.08	
M_1	0.88 ± 0.12	M_\odot
M_2	0.76 ± 0.11	M_\odot

A summary of these results are given in Table 2.

5 DISCUSSION

5.1 Emission line features

Fig. 5 shows single peaked emission lines such as H α , HeI and CaII. The single-peaked HeI 5875 and 6678 Å and H α 6563 Å emission lines are also seen in Thorstensen (2020, Fig. 8). Horne & Marsh (1986) showed that for a high-inclination accreting binary, double-peaked emission lines would be expected. Similarly, Savoury et al. (2012) see double peaks for each of these features due to the disc rotation.

These features may be explained if the WD possesses a strong magnetic field. Polars contain no disc, and therefore emission lines are single-peaked. However, Thorstensen (2020) observed outbursts from LAMOST 0359, classifying the star as a Z Cam dwarf nova. This implies the presence of a disc and rules out the possibility of

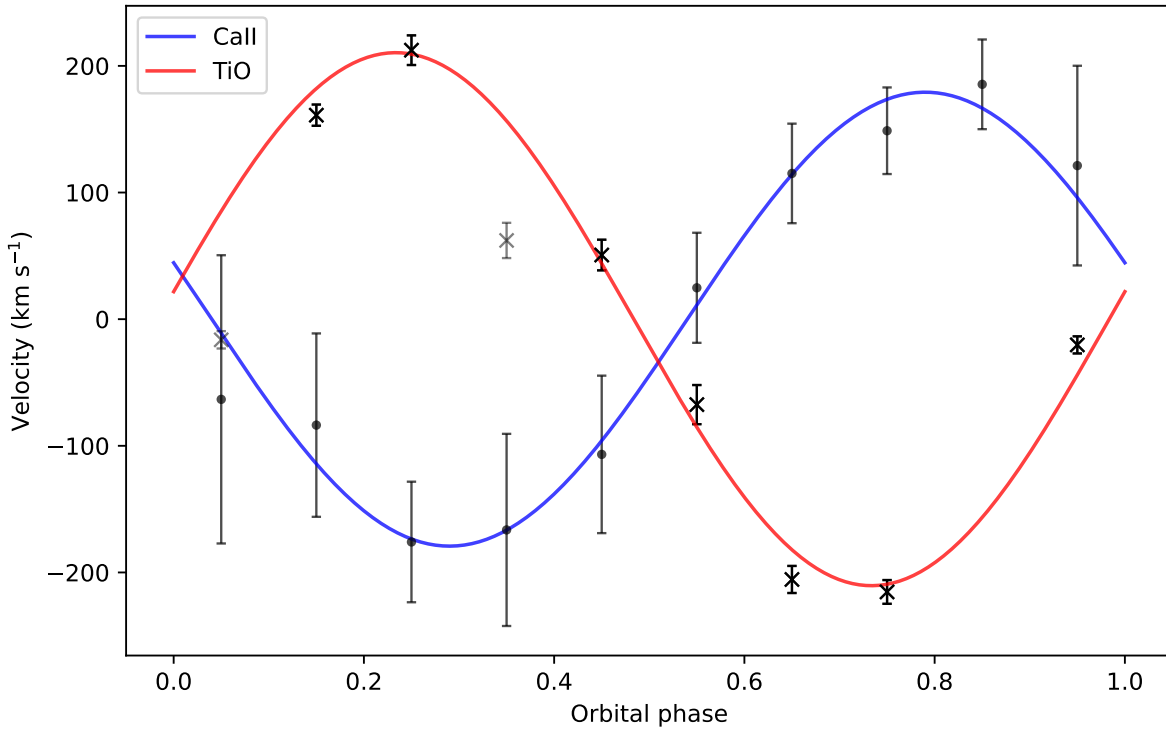


Figure 6. Radial velocity curves of the CaII and TiO lines. The systemic velocities of both fits were subtracted to center both sinusoids on 0 km s^{-1} . The strong black points marked with a cross are the radial velocities determined from the cross-correlation of the TiO absorption features with the M1 Kesseli template. Points unused in the fit ($\phi = 0 - 0.1$ and $\phi = 0.3 - 0.4$) are shown as grey crosses. The fit to these radial velocities is shown with a solid red curve. The faint black points marked with a dot show the radial velocities of the CaII emission features which were measured from the model shift. The fit to these values is shown by the solid blue curve. From visual inspection, it is evident that the errors on the CaII radial velocities are overestimated and the errors on the TiO radial velocities are underestimated.

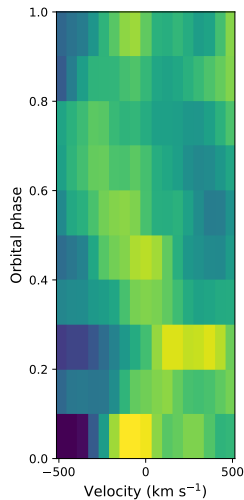


Figure 7. Cross-correlation of the TiO region. Each row in the trail represents the cross-correlation values of each phase binned spectrum. The sinusoidal shape of the peak values of the cross-correlation, shown in yellow, clearly indicate a radial velocity shift.

LAMOST 0359 being a polar. The spectra of [Thorstensen \(2020\)](#) also show no signs of HeII emission at 4685 \AA . From these observations, it is unlikely that LAMOST 0359 is magnetic.

Another possible explanation for the single-peaked emission lines is that there is a wind emerging from the disc. [Murray & Chiang \(1997\)](#) show that if a thin disc is heated by a central source then broad, single-peaked emission lines are produced due to the additional outward velocity of the emanating material.

5.2 Radial velocities

The measured value of K_2 is in agreement with that of [Thorstensen \(2020\)](#), who obtained a value of $K_2 = 215 \pm 28 \text{ km s}^{-1}$ from cross-correlation with a type M1 star template. No value of K_1 is given. Templates in the range K4 – M8 were also cross-correlated. From the K7 – M3 templates, significant sinusoids are seen in the shifts of the cross-correlation peaks, similar to Fig. 7. However, the radial velocities obtained from these fits varied significantly. Radial velocity measurements from these fits are in the range $187 - 216 \text{ km s}^{-1}$. No variation should be seen between templates (e.g. [Littlefair et al. 2023](#)), indicating that there is a systematic error in the radial velocity measurements from cross-correlation of the TiO bands. One source of this error may be a lack of data points used in the fit, due to the phase-binning of spectra and iterative fitting method. Due to the

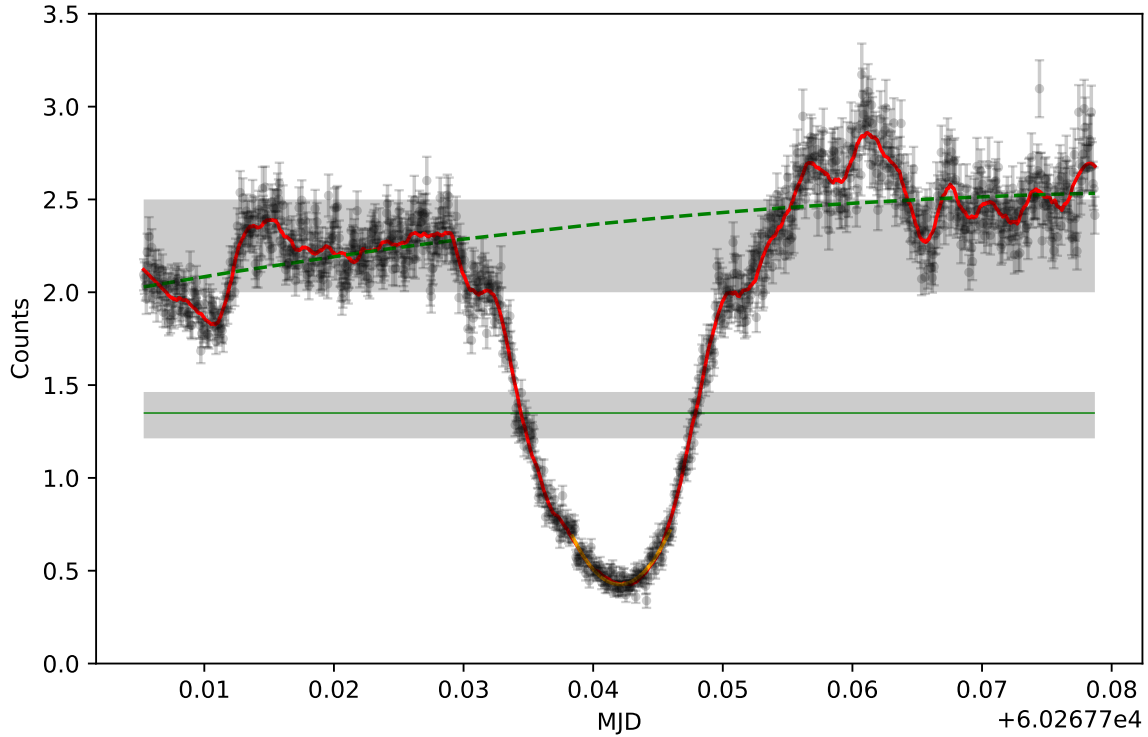


Figure 8. The lightcurve of LAMOST 0359, see Section 2 for observing details. The data are shown as faint black points. The lightcurve was smoothed using a Savitzky-Golay filter, which is shown by the solid red line. The yellow curve shows a Gaussian fit to the trough of the eclipse. The grey bands show the range of continuum level estimates (top) and the corresponding mid-light level (bottom). The dashed green line shows a low-order polynomial fit to the continuum, which crosses the smoothed data within the estimated continuum values. The solid green line shows the mid-light level calculated from the continuum fit, which is in good agreement with the estimated range.

absence of strong NaI, KI or CaII absorption features, the TiO bands were used for cross-correlation despite the telluric absorption in this region.

The measurement of K_2 was affected by the poor S/N of the data. Phase-binning the 60 spectra into 10 bins greatly reduced the resolution of these results. No radial velocity value could be found for the ninth phase-bin ($\phi = 0.8 - 0.9$) as a fit to the peak of the cross-correlation curve was not possible. Cross-correlation of the phase-bins $\phi = 0 - 0.1$ and $\phi = 0.3 - 0.4$ yielded radial velocities which were greater than 50 km s^{-1} away from the initial fit to equation (1). These three bins were therefore excluded in the final fit, and only seven were used. Similarly, fits to the CaII peak at 8662 \AA could not be found for the individual spectra so the 10 phase-bins were used, resulting in 10 radial velocity values to fit.

Systemic velocities of $\gamma = 205 \pm 9 \text{ km s}^{-1}$ and $\gamma = -58 \pm 9 \text{ km s}^{-1}$ were measured from fits to equation (1). These systemic velocity measurements differ greatly between the sinusoidal fits to the CaII and TiO velocity shifts. This suggests that there may have been a systematic error in the wavelength calibration described in Section 3. The most likely source of this error is the shape of the polynomial fit which determines the wavelength-pixel relationship. If the shape is incorrect, an offset in wavelength would be applied to each spectrum during the wavelength calibration. As this offset is the same for each of the spectra, the wavelength shifts used to calculate radial velocities are unaffected.

5.3 Comparison with models

As there are no obvious points of WD ingress and egress in Fig. 8, it was not possible to measure M_2 using a lightcurve model. However, it was possible to test the CV evolution model. Fig. 10 shows the standard model of CV evolution (e.g. Knigge et al. 2011; McAllister et al. 2019). Masses measured by the Sheffield group are shown in black and from other groups' studies in red. The value of M_2 from this paper is in good agreement with the standard model and supports the model's validity at longer periods.

The measured component masses in Table 2 rely on the assumption that the CaII emission triplet originates from the inner disc, and therefore traces the motion of the WD. Fig. 6 shows that the CaII and TiO features are in anti-phase, suggesting that the assumption is valid. However, the sinusoidal fits for both spectral lines show that the phase difference is actually 0.556. It is possible therefore, that the measured value of K_1 is not representative of the WD motion. Observations with higher spectral resolution and S/N would allow for a measurement of the rotational broadening, $v \sin i$. This measurement could then be used to determine the component masses without relying on K_1 (e.g. Smith et al. 1998).

As the points of WD ingress and egress were not visible in Fig. 8, $\Delta\phi_{1/2}$ was estimated by finding the width of the smoothed lightcurve at half-light. The continuum level was estimated by-eye using maximum and minimum values. A fit to the continuum validated these

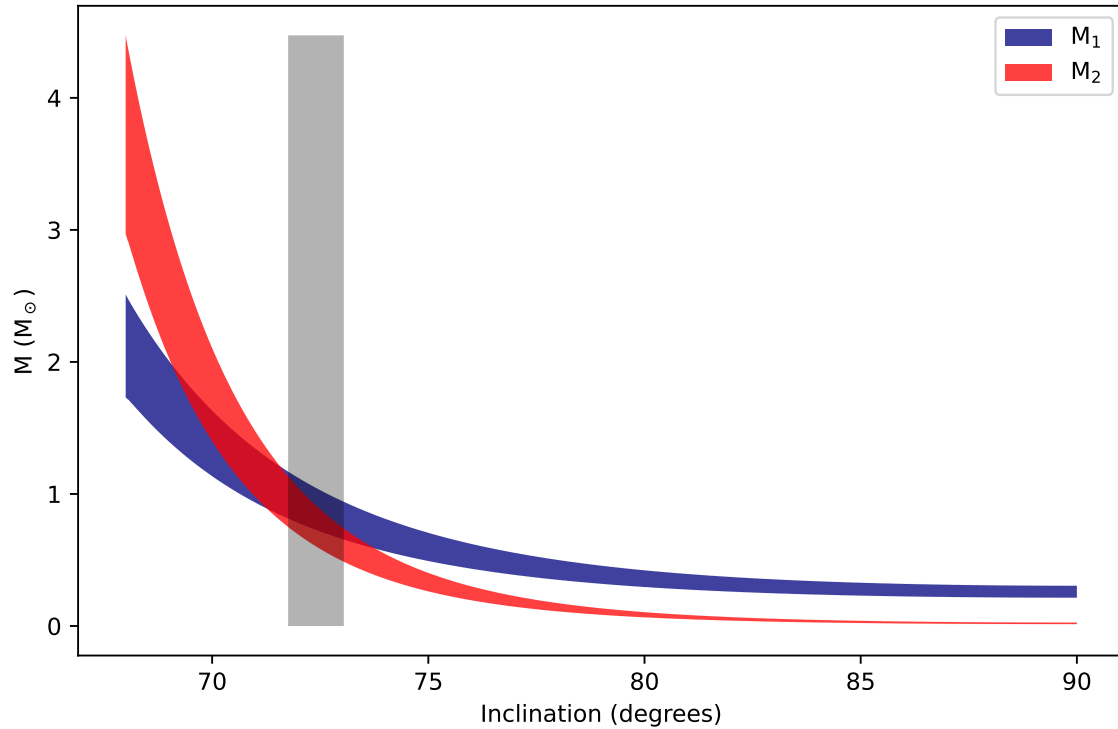


Figure 9. Component masses of LAMOST 0359 as a function of inclination. The primary and secondary masses are shown by the blue and red bands respectively. The grey band indicates the inclination value which was calculated under the assumption that $K_1 = K_{WD}$.

estimates by producing the same values for $\Delta\phi_{1/2}$. However, without visible points of WD ingress and egress in the lightcurve, the measurement of $\Delta\phi_{1/2}$ is a source of systematic error in these radial velocity measurements. Future photometric observations of LAMOST 0359 may yield lightcurves with detectable WD ingress and egress points. These would result in an improved measurement of $\Delta\phi_{1/2}$ and avoid a source of systematic error within the mass determination method.

5.4 Donor star spectral type

By cross-correlating the phase-binned spectra with the Kesseli templates, it was found that the type M1 spectral template was the best fit to the data. However, the measured mass of $M_2 = 0.76 \pm 0.11 M_\odot$ is not typical of this spectral class. For a main-sequence-like donor star, the temperature expected of an M1 dwarf is significantly cooler than is implied by the measured mass from this study (Pecaut et al. 2012). From the standard model of CV evolution (Knigge et al. 2011) the implied temperature of 3800 K corresponds to an M0 star, which is in good agreement with the M1 estimate and suggests that the donor star is in thermal equilibrium. The measured donor mass $M_2 = 0.76 \pm 0.11 M_\odot$ is within 2 errorbars of the standard model shown in Fig. 10. The measurement of K_2 is consistent with the value obtained by Thorstensen (2020), despite the scarcity of data points. Furthermore, the systematic error from the wavelength calibration is unlikely to affect the amplitudes of the radial velocity fits in Fig. 6. The mild discrepancy between this measurement of M_2 and the

model in Fig. 10 is likely due to systematic errors which arose from the determination of $\Delta\phi_{1/2}$ from the lightcurve in Fig. 8 and the assumption that $K_1 = K_{WD}$.

6 CONCLUSIONS

The measurement of the donor mass $M_2 = 0.76 \pm 0.11 M_\odot$ is in good agreement with the CV evolution model of Knigge et al. (2011). This study provides evidence that the standard model of CV evolution holds for long-period systems above the period gap, where there are few observed systems (see Fig. 10). It was not possible to test lightcurve models as there are no visible points of WD ingress and egress in Fig. 8. Despite the small number of data points available for the radial velocity curves in Fig. 6, the measured radial velocity of the donor $K_2 = 211 \pm 12 \text{ km s}^{-1}$ is in good agreement with Thorstensen (2020). It is also found that the M1 spectral template is the best fit to this data.

Single-peaked emission lines suggest that radiation from the WD illuminates the disc creating winds which emanate outwards. (Murray & Chiang 1997). This additional velocity component prevents double-peaked emission lines which are typically seen in rotating discs (Horne & Marsh 1986). The WD is unlikely to be strongly magnetic as LAMOST 0359 has been observed to outburst, and its spectra show no signs of HeII emission.

The values of M_1 and M_2 rely on two assumptions: that the CaII emission peaks trace the motion of the WD; and that $\Delta\phi_{1/2}$ is given by the width of the lightcurve at half-light. Spectra with higher spectral

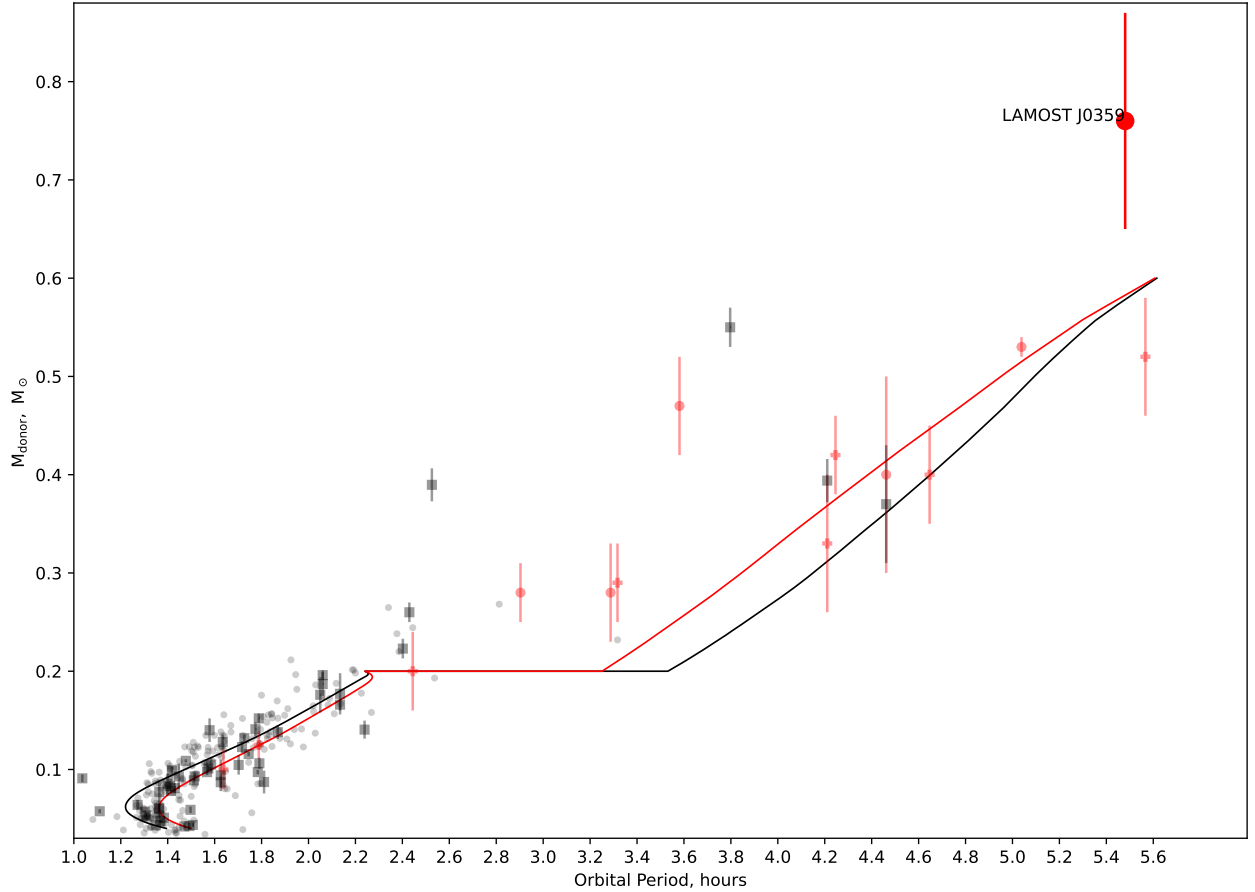


Figure 10. The standard model of CV evolution is represented by a solid black line, and an updated model with additional AM loss (Knigge et al. 2011) is shown by the solid red line. The grey squares represent photometric masses obtained by eclipse modelling by the Sheffield group using multicolour data. The red circles show masses obtained by eclipse modelling from other groups who do not use multicolour data. The red plus symbols show masses measured by other groups using the donor radial velocities. The grey circles show superhumpers.

resolution and S/N of LAMOST 0359 would allow a more accurate measurement of M_2 , and determine the level of agreement with the CV evolution model in Fig. 10. Furthermore, measurements of the rotational broadening $v \sin i$ would give improved values for the component masses without the assumptions required of this paper. These independent measurements would greatly improve the mass determination method from this paper and provide important tests of the CV evolution model for long-period systems.

ACKNOWLEDGEMENTS

I would like to thank my supervisor, Dr Stuart Littlefair, for his extensive support and guidance throughout this project. I would also like to thank the staff at the Isaac Newton Group of Telescopes. In particular Judith Santos and Jacco Terwel, who were my company on my very first night as a support astronomer and my friends thereafter, for their observations of LAMOST 0359 in September 2023. This work is based on discretionary-time observations made with the Isaac Newton Telescope operated on the island of La Palma by the Isaac Newton Group of Telescopes in the Spanish Observatorio del Roque de los Muchachos of the Instituto de Astrofísica de Canarias.

DATA AVAILABILITY

The data underlying this article will be shared on reasonable request to the corresponding author.

REFERENCES

- Angel J. R. P., 1978, *Annual Review of Astronomy and Astrophysics*, 16, 487
- Bailey J., 1979, *Monthly Notices of the Royal Astronomical Society*, 187, 645
- Buat-Ménard V., Hameury J.-M., Lasota J.-P., 2001, *Astronomy & Astrophysics*, 366, 612
- Clough S. A., Shephard M. W., Mlawer E. J., Delamere J. S., Iacono M. J., Cady-Pereira K., Boukabara S., Brown P. D., 2005, *Journal of Quantitative Spectroscopy and Radiative Transfer*, 91, 233
- Cook M. C., Warner B., 1984, *Monthly Notices of the Royal Astronomical Society*, 207, 705
- Copperwheat C. M., Marsh T. R., Dhillon V. S., Littlefair S. P., Hickman R., Gänsicke B. T., Southworth J., 2010, *Monthly Notices of the Royal Astronomical Society*, 402, 1824
- Dhillon V. S., et al., 2014, *Monthly Notices of the Royal Astronomical Society*, 444, 4009
- Garraffo C., Drake J. J., Alvarado-Gomez J. D., Moschou S. P., Cohen O., 2018, *The Astrophysical Journal*, 868, 60

- Godon P., Sion E. M., 2022, *The Astrophysical Journal*, 928, 26
- Gullikson K., Dodson-Robinson S., Kraus A., 2014, *The Astronomical Journal*, 148, 53
- Hellier C., 2001, *Cataclysmic Variable Stars - How and Why They Vary*. Springer Science & Business Media
- Hind J. R., 1856, *Monthly Notices of the Royal Astronomical Society*, 16, 56
- Horne K., 1986, *Publications of the Astronomical Society of the Pacific*, 98, 609
- Horne K., Marsh T. R., 1986, *Monthly Notices of the Royal Astronomical Society*, 218, 761
- Horne K., Welsh W. F., Wade R. A., 1993, *The Astrophysical Journal*, 410, 357
- Horne K., Marsh T. R., Cheng F. H., Hubeny I., Lanz T., 1994, *The Astrophysical Journal*, 426, 294
- Hou W., Luo A.-L., Li Y.-B., Qin L., 2020, *The Astronomical Journal*, 159, 43
- Kesseli A. Y., West A. A., Veyette M., Harrison B., Feldman D., Bochanski J. J., 2017, *The Astrophysical Journal Supplement Series*, 230, 16
- Knigge C., Baraffe I., Patterson J., 2011, *The Astrophysical Journal Supplement Series*, 194, 28
- Lam M. C., Smith R. J., Arcavi I., Steele I. A., Veitch-Michaelis J., Wyrzykowski L., 2023, *The Astronomical Journal*, 166, 13
- Littlefair S. P., Dhillon V. S., Marsh T. R., Gänsicke B. T., Southworth J., Baraffe I., Watson C. A., Copperwheat C., 2008, *Monthly Notices of the Royal Astronomical Society*, 388, 1582
- Littlefair S. P., Rodríguez-Gil P., Marsh T. R., Parsons S. G., Dhillon V. S., 2023, *Monthly Notices of the Royal Astronomical Society*
- Marsh T. R., 1989, *Publications of the Astronomical Society of the Pacific*, 101, 1032
- McAllister M., et al., 2019, *Monthly Notices of the Royal Astronomical Society*, 486, 5535
- Murray N., Chiang J., 1997, *The Astrophysical Journal*, 474, 91
- Osaki Y., 1974, *Publications of the Astronomical Society of Japan*, 26, 429
- Paczynski B., Sienkiewicz R., 1983, *The Astrophysical Journal*, 268, 825
- Pala A. F., et al., 2020, *Monthly Notices of the Royal Astronomical Society*, 494, 3799
- Pecaut M. J., Mamajek E. E., Bubar E. J., 2012, *The Astrophysical Journal*, 746, 154
- Pickering E. C., Wells L. D., 1896, *The Astrophysical Journal*, 3, 77
- Pogson N., 1857, *Monthly Notices of the Royal Astronomical Society*, 17, 200
- Rappaport S., Verbunt F., Joss P. C., 1983, *The Astrophysical Journal*, 275, 713
- Savitzky A., Golay M. J. E., 1964, *Analytical Chemistry*, 36, 1627
- Savory C. D. J., Littlefair S. P., Dhillon V. S., Marsh T. R., Copperwheat C. M., Kerry P., Hickman R. D. G., Parsons S. G., 2011, *Monthly Notices of the Royal Astronomical Society*, 415, 2025
- Savory C. D. J., Littlefair S. P., Marsh T. R., Dhillon V. S., Parsons S. G., Copperwheat C. M., Steeghs D., 2012, *Monthly Notices of the Royal Astronomical Society*, 422, 469
- Schreiber M. R., et al., 2010, *Astronomy & Astrophysics*, 513, L7
- Schreiber M. R., Zorotovic M., Wijnen T. P. G., 2016, *Monthly Notices of the Royal Astronomical Society: Letters*, 455, L16
- Smak J., 1980, *Symposium - International Astronomical Union*, 88, 443
- Smith R. C., 2006, *Contemporary Physics*, 47, 363
- Smith D. A., Dhillon V. S., Marsh T. R., 1998, *Monthly Notices of the Royal Astronomical Society*, 296, 465
- Song Q., Zhang T., Wang Z., Zhang S., Yang L., 2018, *Applied Optics*, 57, 6876
- Spark M. K., O'Donoghue D., 2015, *Monthly Notices of the Royal Astronomical Society*, 449, 175
- Spruit H. C., Ritter H., 1983, *Astronomy and Astrophysics*, 124, 267
- Starrfield S., Sparks W. M., Truran J. W., Shaviv G., 1989, *NASA STI/Recon Technical Report N*, 90, 19931
- Tapia S., 1977, *The Astrophysical Journal*, 212, L125
- Thorstensen J. R., 2020, *The Astronomical Journal*, 160, 151
- Warner B., 1995, *Cataclysmic Variable Stars*. Cambridge Astrophysics, Cambridge University Press, Cambridge, doi:10.1017/CBO9780511586491
- Wood J. H., Irwin M. J., Pringle J. E., 1985, *Monthly Notices of the Royal Astronomical Society*, 214, 475
- Wood J., Horne K., Berriman G., Wade R., O'Donoghue D., Warner B., 1986, *Monthly Notices of the Royal Astronomical Society*, 219, 629
- Wright N. J., Drake J. J., 2016, *Nature*, 535, 526
- Zorotovic M., Schreiber M. R., Gänsicke B. T., 2011, *Astronomy and Astrophysics*, 536, A42
- Zorotovic M., et al., 2016, *Monthly Notices of the Royal Astronomical Society*, 457, 3867

APPENDIX A: RELATIONSHIP TO PREVIOUS WORK

An observing proposal for time on the 2.5-m Isaac Newton Telescope at the Roque de los Muchachos observatory in La Palma was accepted in June 2023 and the observations were performed on the nights of the 8th, 9th and 11th of September 2023. No work was done for this project using this data before the beginning of the academic year.

This paper has been typeset from a \LaTeX file prepared by the author.